Scale interactions and anisotropy in stable boundary layers

Nikki Vercauteren, Vyacheslav Boyko, Davide Faranda, Ivana Stiperski

ORIGINAL ARTICLE

Journal Section

Scale interactions and anisotropy in stable boundary layers

Nikki Vercauteren[1] | **Vyacheslav Boyko**[1] | **Davide Faranda**[2] | **Ivana Stiperski**[3]

[1]FB Mathematik und Informatik, Freie Universitaet Berlin, 14195 Berlin, Germany

[2]LSCE-IPSL, CEA Saclay l'Orme des Merisiers, CNRS UMR 8212 CEA-CNRS-UVSQ, Universite Paris-Saclay, 91191 Gif-sur-Yvette, France

[3]Institute of Atmospheric and Cryospheric Sciences, University of Innsbruck, Innsbruck, Austria

Correspondence
Nikki Vercauteren, FB Mathematik und Informatik, Freie Universitaet Berlin, 14195 Berlin, Germany
Email: nikki.vercauteren@fu-berlin.de

Present address
[†]FB Mathematik und Informatik, Freie Universitaet Berlin, 14195 Berlin, Germany

Funding information
Deutsche Forschungsgemeinschaft (DFG), Grant Number: VE933-2/1; Austrian Science Fund (FWF), Grant Number: T781-N32

Abbreviations:

* Equally contributing authors.

Regimes of interactions between motions on different timescales are investigated in the FLOSSII dataset for nocturnal near-surface stable boundary layer (SBL) turbulence. The nonstationary response of turbulent vertical velocity variance to non-turbulent, sub-mesoscale wind velocity variability is analysed using the bounded variation, finite element, vector autoregressive factor models (FEM-BV-VARX) clustering method. Several locally stationary flow regimes are identified with different influences of sub-meso wind velocity on the turbulent vertical velocity variance. In each flow regime, we analyse multiple scale interactions and quantify the amount of turbulent variability which can be statistically explained by the individual forcing variables. The state of anisotropy of the Reynolds stress tensor in the different flow regimes is shown to relate to these different signatures of scale interactions. In flow regimes dominated by submesoscale wind variability, the Reynolds stresses show a clear preference for strongly anisotropic, one-component stresses, which tend to correspond to periods in which the turbulent fluxes are against the mean gradient. These periods additionally show stronger persistency in their dynamics, compared to periods of more isotropic stresses. The analyses give insights on how the different topologies relate to nonstationary turbulence triggering by sub-mesoscale motions.

KEYWORDS
statistical clustering, regime detection, nonstationary turbulence, nocturnal boundary layer, submeso motions, anisotropy tensor, persistent dynamics

1 | INTRODUCTION

Nocturnal and stable boundary layers (SBL) represent a challenge to numerical weather prediction (Sandu et al., 2013; Holtslag et al., 2013). Difficulties arise due to the unsteady nature of the flow caused by the interactions of processes on multiple scales. In strong wind conditions, mechanical forcing of turbulence is enough to overcome buoyant damping and turbulence is generally continuous and rather well described by classical similarity theory. In weak-wind conditions however, sporadic turbulence can be triggered by localised shear accelerations due to sub-mesoscale motions such as internal gravity waves, density currents, wind gusts or other motions (Sun et al., 2004; Mahrt, 2014; Sun et al., 2015; Mortarini et al., 2017). The non-turbulent, small-scale motions take a variety of forms and are poorly understood and not represented in models (Belušić and Güttler, 2010; Kang et al., 2015; Lang et al., 2017). Such non-local scale interactions modify the characteristics of boundary layer turbulence, giving it an intermittent nature, with a tendency to be decoupled from the surface (Acevedo et al., 2015). In this very stable regime, classical surface-based parameterisations of turbulence fail at representing turbulence resulting from interactions with non-turbulent unsteady flow accelerations.

Non-stationary turbulence under the influence of submeso motions has been analysed with different data analysis methods (Mahrt et al., 2012b; Mahrt and Thomas, 2016; Cava et al., 2016; Mortarini et al., 2017). A method to classify flow regimes based on the influence of submeso motions has been proposed recently using the FEM-BV-VARX method (Horenko, 2010b), which provides the means of objectively classifying non-stationary dynamics influenced by external variables. This statistical clustering technique has proven powerful for classifying large scale atmospheric flow data, e.g. for identifying global atmospheric circulation regimes and blockings (O'Kane et al., 2016; Risbey et al., 2015). In the case of SBL turbulence, a combination of multiscale data filtering and FEM-BV-VARX clustering, was used by Vercauteren and Klein (2015) and Vercauteren et al. (2016) to characterise the interactions between sub-mesoscale non-turbulent motions and turbulence. This strategy was found to successfully identify periods in which non-turbulent motions dominate the turbulence dynamics, corresponding to very stable periods.

As an additional effect on the structure of turbulence, stable temperature stratification results in a strong attenuation of the vertical turbulent motions by buoyancy forces, while shear forcing exerts a straining action. The combination of these effects can lead to strongly anisotropic turbulence (Smyth and Moum, 2000). Turbulence anisotropy leads to additional difficulties in parameterising turbulence, and Stiperski and Calaf (2018) have recently given a new perspective on the failure of traditional similarity scaling by relating it to the topology of the Reynolds stress tensor, based on observational evidence. Anisotropy of the energy-containing scales is quantified using the anisotropy stress tensor and the structure of the tensor can be conveniently represented using two invariants (Lumley, 1978). Based on the eigenvalues of the anisotropy tensor, one can classify turbulence according to three limiting states (Pope, 2000). The one-component limiting state describes a flow where one eigenvalue is much larger than the other two (sometimes referred to as rod-like turbulence), while the two-component limit has two directions with equal magnitude (and is sometimes referred to as pancake-like turbulence) and all three directions have equal magnitude in the three component, isotropic limit. Stiperski and Calaf (2018) showed that while close to isotropic and close to two-component axisymmetric stresses agreed well with existing SBL scaling relationships, one-component axisymmetric stresses deviated strongly from similarity scaling.

Delineating isotropic from one or two-component cases appeared possible by using a combination of the wind speed and the turbulent kinetic energy (TKE), but differentiating between the one- and two-component cases themselves appeared more difficult. The delineation based on the wind speed and TKE is the approach taken by the Hockey Stick Transition (HOST) framework (Sun et al., 2015), based on the observation that turbulence shows two distinct behaviours depending on the wind speed. The low wind speed part of the HOST framework corresponds to intermittent turbulence where the TKE is quasi-invariant with the mean wind speed, and where the Reynolds stress tensor is highly anisotropic (Stiperski and Calaf, 2018). This regime is also characterised by the presence of myriads of anisotropic sub-mesoscale motions which act as trigger for turbulence. The combination of multiple scale analysis of turbulence and statistical clustering proposed by Vercauteren and Klein (2015) and Vercauteren et al. (2016) allows to identify flow regimes in which scales interact differently, and the regimes may correspond to different states of anisotropy.

The forcing of turbulence by wave-like non-turbulent motions typically occurs on scales just above the turbulent scales. In the Kolmogorov view of turbulence, the cascade of energy from large to small scales is accompanied by a loss of information about the geometry of the large scales. The unsteady forcing may result in non-equilibrated, highly anisotropic turbulence as indicated by multiscale decompositions in Vercauteren et al. (2016). According to the theory, highly anisotropic turbulence should tend to equilibrate to quasi-isotropic states at the small scales (Pope, 2000). The dynamical evolution of large scale anisotropic structures towards isotropy is however a subject of research, which can be studied based on the anisotropy tensor structure. Choi and Lumley (2001) showed experimental evidence that the rate of return to isotropy depends on the initial topological state and is very slow for cigar-shaped, axisymmetric turbulence at a high Reynolds number. Their analyses also showed that the turbulence trajectories to isotropy are nonlinear. Brugger et al. (2018) analysed the route to isotropy based on atmospheric measurements in the surface layer for canopy flows and highlighted a large influence of thermal stratification. Their analyses showed that trajectories in the phase space (for decreasing scales) defined by the anisotropy invariants deviate from those of return-to-isotropy known for homogeneous turbulence. In stably stratified conditions, the influence of anisotropic sub-mesoscale motions probably affects the turbulence anisotropy dynamics and this topic deserves investigation.

A way to investigate the dynamical evolution of turbulence depending on its initial topology is to consider the dynamics in the anisotropy phase space defined by the invariants of the anisotropy tensor. Lucarini et al. (2016) recently developed indicators that proved able to quantify the persistence of dynamics in phase space as well as the local dimension of the dynamics and applied them in the context of climate dynamics (Faranda et al., 2017a; Messori et al., 2017). Quantifying the persistence of the turbulent states depending on their topology informs us on how constrained or not the dynamical evolution of turbulence is in a given starting state of anisotropy. Quantifying the dimension of the dynamics at each point of the anisotropy phase space additionally enables us to investigate the existence of preferred directions of the evolution of turbulent states of anisotropy.

In this work we will focus on following questions: Do flow regimes separated according to their scale interactions properties correspond to unique states of anisotropy? How persistent are different states of anisotropy and is there a preferred trajectory in the anisotropy phase space in stably stratified conditions? We will address these questions based on turbulence measurements from the Fluxes Over Snow Surfaces II campaign (FLOSSII).

2 | METHODS

2.1 | Dataset

The analysis is based on turbulence data collected during the Fluxes Over Snow Surfacess II (FLOSSII) experiment that was conducted from 20 November 2002 to 4 April 2003 over a locally flat grass surface south of Walden, Colorado,

USA, in the Arapaho National Wildlife Refuge (Mahrt and Vickers, 2005). The surface was often covered by a thin snow layer during the field program. The turbulence is measured by a tower collecting data at 1, 2, 5, 10, 15, 20 and 30 m with Campbell CSAT3 sonic anemometers. The data set was quality controlled and segments of instrument problems and meteorologically impossible values were eliminated (Larry Mahrt, personal communication).

The following analysis is based on night-time data, taken between 18:00 and 7:00, Local Standard Time. The period is selected because the surface sensible heat flux averaged over all nights is negative during this time. Flow regime identification based on the FEM-BV-VARX clustering methodology (see Section 2.3) ideally requires continuous data, however the dataset will consist of continuous night-time data separated by gaps during the day. In order to maximise continuity of the dataset, nights with data gaps longer than 80 minutes (12 nights) as well as nights with wind flowing persistently through the measurement tower for periods longer than 5 minutes (51 nights) were removed from the analysis. The resulting 68 nights left for analysis have data gaps shorter than 1 minute and are deemed mostly uncontaminated. The short gaps are linearly interpolated. The 60Hz raw data are rotated into the mean wind direction based on 30 minutes average using Double Rotation.

The flow characteristics of the FLOSSII dataset were analysed by Mahrt (2011), showing complex nonstationary relationships between turbulence and sub-mesoscale wind velocity that will be analysed with the objective FEM-BV-VARX classification strategy here. Analyses of non-turbulent structures identified as sub-mesoscale motions by the Turbulent Event Detection (TED) method (Kang et al., 2015) revealed the presence of complex structures affecting the turbulent dynamics.

2.2 | Extracting scales of motion

The multiresolution flux decomposition (MRD) (Vickers and Mahrt, 2003) and other wavelet analysis tools have been successfully used to analyse SBL scale-wise properties of flux. The MRD can be used to assess the amount of flux that is due to eddies of a certain size, thereby providing a way to identify a cospectral gap scale. The gap scale is usually identified as the scale at which the flux crosses the zero-line and indicates the appropriate averaging period needed to separate contributions of non-turbulent sub-mesoscales of motion from turbulent fluxes. The MRD analyses of the nocturnal FLOSSII data show that the cospectral gap scale depends on the flow regime (this topic will be discussed in Section 3.1 and is illustrated in Fig. 4), but that scales smaller than approximately 1 minute mainly correspond to turbulent fluxes. We therefore define the turbulent vertical velocity fluctuations as $\sigma_w = \sqrt{\overline{w'w'}}$, where w is the vertical wind velocity component, the overbar denotes an averaging period of 1 minute and the prime denotes deviations from the average. A sub-mesoscale mean wind speed is defined as:

$$V_{smeso} = \sqrt{u_s^2 + v_s^2}, \tag{1}$$

where u_s and v_s are the streamwise and lateral velocity components on sub-mesoscales. In the definition of the sub-mesoscale fluctuations $\phi_s = \overline{\phi} - [\phi]$, the overbar denotes a 1-min averaging time and the square brackets denote a 30-min averaging time, such that these fluctuations represent the deviations of the 1-min sub-record averages from the 30-min average. These definitions of turbulent vertical velocity fluctuations and sub-mesoscale wind velocity fluctuations are used to analyse the non-stationary interactions between submeso motions and turbulence. This choice of timescales is identical to the choice made by Vercauteren and Klein (2015) and Vercauteren et al. (2016) to analyse scale interactions in the SnoHATS dataset of SBL turbulence.

2.3 | Clustering flow regimes

The Finite Element, Bounded Variation, Vector Auto-Regressive with eXternal factors (FEM-BV-VARX) method (Horenko, 2010a,b) relates an observed variable of interest at a discrete-time t (in our context $\sigma_w(t)$) to the past history of observations ($\sigma_w(t - p\tau)$, where $p \in \mathbb{Z}_{>0}$ and τ is the discrete-time unit step equal to the inverse sampling frequency). Influences from external forcing variables can also be considered. When using the FEM-BV-VARX method, we assume that the evolution in time of the turbulent mixing can be approximated by a locally stationary statistical process (VARX) that is influenced by the horizontal wind speed at specified sub-mesoscales of motion. The method is thus applied to identify different SBL flow regimes, based on the interactions of different scales of motion. The VARX model relates the dynamics of $\sigma_w(t)$ to the external factors $V_{smeso}(t - p\tau)$, and the relationship is modulated by a set of time-dependent parameters $\overline{\Theta}(t)$. The VARX model in our application takes the following form:

$$\sigma_w(t) = \mu(t) + B_0(t)V_{smeso}(t) + B_1(t)V_{smeso}(t - \tau) + \cdots + B_p(t)V_{smeso}(t - p\tau) + C(t)\varepsilon(t)\,, \tag{2}$$

where the process $\sigma_w(t)$ is the time evolution of the vertical velocity variance measured at one location; the external factor is the time evolution of the streamwise velocity on our previously defined sub-mesoscales V_{smeso} (Eq. 1). ε_t is a noise process with zero expectation, the parameters $\overline{\Theta}(t) = (\mu(t), B(t), C(t))$ are time- dependent matrix coefficients for the process and p is the memory depth of the external factor. The model assumes a linear relationship between σ_w and V_{smeso}, which was shown to be appropriate by Mahrt (2011), based on the FLOSSII dataset and by Vercauteren and Klein (2015) for the SnoHATS dataset. Both analyses however highlighted that the linear dependence of σ_w on the sub-mesoscale wind speed is not always constant. The turbulence relates to different scales of motions in a complex, non-stationary way and we use the FEM-BV-VARX clustering method to disentangle the different relationships. Since our interest lies mainly in characterizing scale interactions, we do not consider an autoregressive part in the model (2). The number of statistical processes corresponds to the number of clusters. The assumption of local stationarity of the statistical process is enforced by setting a persistence parameter C_p, which defines the maximum allowed number of transitions between K different statistical processes (corresponding to different values of the matrix coefficients $\overline{\Theta}(t)$). The cluster states are indicated by a cluster affiliation function, which is calculated by the procedure. The reader is referred to Horenko (2010b) for information regarding the minimisation procedure used to solve the clustering problem. More detailed explanations on the application of the classification scheme to SBL turbulence is given in Vercauteren and Klein (2015). User defined parameters and their choice are discussed in the results section 3.1.

2.4 | Anisotropy of the Reynolds stress tensor

The forces imposed on the mean flow by the turbulent fluctuations are quantified using the Reynolds stress tensor

$$\overline{u_i' u_j'} = \begin{pmatrix} \overline{u_1' u_1'} & \overline{u_1' u_2'} & \overline{u_1' u_3'} \\ \overline{u_2' u_1'} & \overline{u_2' u_2'} & \overline{u_2' u_3'} \\ \overline{u_3' u_1'} & \overline{u_3' u_2'} & \overline{u_3' u_3'} \end{pmatrix}, \tag{3}$$

where u_i' denotes velocity fluctuations and the overbar represents time average, i.e. $u_i' = u_i - \overline{u_i}$. The anisotropic components of the tensor effectively transport momentum, while the isotropic or diagonal components can be absorbed in a modified mean pressure (Pope, 2000). A way to characterise anisotropy of turbulence is to use symmetric, traceless

tensors whose elements vanish in isotropic flows. The anisotropy tensor

$$a_{ij} = \frac{\overline{u_i u_j}}{2k} - \frac{\delta_{ij}}{3}, \quad k = \frac{\overline{u_i u_i}}{2}, \tag{4}$$

in which δ is the Kronecker delta and summation over repeated indices is implied, satisfies this condition and was introduced by Lumley (1978) to describe the evolution of turbulence towards isotropy in homogeneous, anisotropic flows. Its two independent principal invariants ($II = a_{ij}a_{ji}$, $III = a_{ij}a_{in}a_{jn}$) quantify the level of anisotropy of turbulent quantities and thus give it a simple graphical representation on a plane, initially proposed by Lumley and Newman (1977). A functional relationship between II and III further defines a bounded region - the *Lumley triangle* - on the plane of the invariants in which all physically realisable turbulence is found. As an equivalent alternative to the Lumley triangle, a Barycentric Lumley map based on a linear domain that equally weighs the different limiting states of anisotropy simplifies the graphical interpretation of anisotropy of turbulence, avoiding nonlinear distortions (Banerjee et al., 2009). The limiting states are placed at $x_{1C} = (1, 0)$, $x_{2C} = (0, 0)$, and $x_{3C} = (1/2, \sqrt{3/2})$, and any anisotropy state is located as a point (x_B, y_B) in this phase space such that the convex linear combination holds (see Fig. 1)

$$x_B = C_{1C}x_{1C} + C_{2C}x_{2C} + C_{3C}x_{3C} = C_{1C} + \frac{1}{2}C_{3C}, \tag{5}$$

$$y_B = C_{1C}y_{1C} + C_{2C}y_{2C} + C_{3C}y_{3C} = \frac{\sqrt{3}}{2}C_{3C}. \tag{6}$$

The corresponding weights (C_{1C}, C_{2C}, C_{3C}) are entirely determined by the eigenvalues of the normalised Reynolds stress anisotropy tensor, such that $C_{1C} = \lambda I - \lambda II$, $C_{2C} = 2(\lambda II - \lambda III)$, and $C_{3C} = 3\lambda III + 1$.

Following Stiperski and Calaf (2018), we define three regions in the Barycentric Lumley map that correspond to anisotropy states close to each of the three pure limiting states. These regions are determined as kite-shaped regions of the Barycentric map illustrated in Figure 1. The limiting lines for each kite were chosen to cover 70 % of the sides of the equilateral triangle. Anisotropy states falling within each of the limiting regions will be denoted as *pure anisotropy states*.

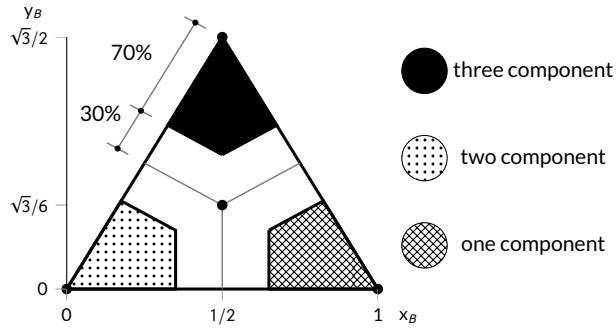

FIGURE 1 Definition of the anisotropy states in the barycentric map.

2.5 | Persistence and dimension of dynamical states of anisotropy

The Lumley triangle or its barycentric map counterpart define a bounded region in a phase space spanned by the two principal invariants of the Reynolds stress anisotropy tensor. All physically realisable turbulence states are found within

this triangle. In the mathematical field of dynamical systems, the geometrical set hosting all the trajectories of a system is defined as the attractor (Eckmann and Ruelle, 1985). Knowledge of the attractor informs on how often and for how long the trajectories of the system visit each region of the phase space and for how long the trajectory stays in the neighbourhood of each point. The behaviour of the system is entirely known if one can define those properties for each point of the attractor. In our set up, we do not dispose of the knowledge of the entire attractor, but we can reconstruct important information on the dynamics via a projection on x_B and y_B. This subset of the attractor is a special Poincaré section because of its physical importance. In a similar fashion as in Faranda et al. (2017b), we will study the dynamical properties of such Poincaré section and try to infer physical information on turbulence.

Our dynamical observables therefore consist of piece wise continuous trajectories of the turbulence anisotropy states defined by $(x_B(t), y_B(t))$, and the Poincaré recurrence theorem enables the analysis of properties of the attracting dynamics based on time series. The Poincaré recurrence theorem essentially states that certain dynamical systems, such as those bound to a finite volume, will after some time return to a state very close to the initial state. The time to return to an initial state depends on its location in phase space, and naturally on the required degree of closeness. A point $(x_B(t), y_B(t))$ in a timeseries of the invariants of the anisotropy tensor corresponds to a point in the attractor (the barycentric map or some part of it), and states whose distance to $(x_B(t), y_B(t))$ is small are the neighbours of that point or state. The density of points around each state, locally in space and time, defines a local dimension of the dynamics. In the barycentric map, the phase-space is the plane defined by the Poincaré section x_B and y_B and is thus two-dimensional. However if some states of anisotropy are visited less than others, locally the dimension of the Poincaré section may be smaller than two. If a trajectory leaves the neighbourhood of an initial state of anisotropy very fast, the persistence of the state will be small. If on the contrary the trajectory remains in the neighbourhood of the initial state for some time, the anisotropy state is more persistent.

Lucarini et al. (2016) recently proposed a methodology to estimate the persistence and local dimension of dynamical states based on timeseries of dynamical observables, combining the Poincaré recurrence theorem with theory of extreme value statistics. In their framework, points on the attractor are characterized by parameters of extreme value probability distributions. For a given initial point ζ on a chaotic attractor, the probability of a dynamical trajectory $x(t)$ to return within a spherical neighbourhood of the initial point has been shown to follow a generalized Pareto distribution (Moreira Freitas et al., 2010), which is a standard distribution in extreme value statistics and is a modified exponential law. The time series in this context is the distance between ζ and the other observations along the trajectory

$$g\left(x(t)\right) = -\log\left(\delta(x(t), \zeta)\right), \tag{7}$$

where $\delta(x, y)$ is a distance function between two points (e.g. the Euclidean distance). Taking the logarithm increases the discrimination of small values of $\delta(x, y)$ and large values of $g(x(t))$ correspond to small distances from the point ζ. The probability of logarithmic returns in the neighbourhood around ζ can then be expressed as

$$P\left(g\left(x(t)\right) > q, \zeta\right) \simeq \exp\left[-\frac{x - \mu(\zeta)}{\sigma(\zeta)}\right], \tag{8}$$

and the parameters of the exponential law μ and σ depend on the point ζ. The local dimension of the dynamics around the point ζ is finally given by (see Lucarini et al. (2016) for proofs and numerical verifications, and Faranda et al. (2017a) for an application to climate dynamics)

$$d(\zeta) = \frac{1}{\sigma(\zeta)} \tag{9}$$

In equation (8), q is an exceedance threshold, and is linked to the radius ϵ of the spherical neighbourhood of ζ via $q = g^{-1}(\epsilon) = exp(-\epsilon)$. In other words, requiring the trajectory to fall within a sphere around the point ζ is equivalent to requiring the series of $g(x(t))$ to be over the threshold q, which can be simply set as a percentile of the series itself.

The quantification of the persistence of the state ζ follows rather intuitively: the longer the dynamical trajectory stays in the spherical neighbourhood of the point ζ, the more persitent is the dynamics in this state. This residence time can be computed by introducing a further parameter θ in the probability distribution (8), known as extremal index:

$$P\left(g\left(x(t)\right) > q, \zeta\right) \simeq \exp\left[-\theta\left(\frac{x-\mu(\zeta)}{\sigma(\zeta)}\right)\right], \tag{10}$$

This parameter θ can be interpreted as the inverse of the mean residence time within the spherical neighbourhood of ζ. From (10) it follows that $0 < \theta < 1$, where low values correspond to high persistence of the trajectory in the neighbourhood of ζ, while values close to 1 imply that the trajectory immediately leaves the sphere (Lucarini et al., 2016).

3 | RESULTS AND DISCUSSION

3.1 | Scale interaction properties in classified flow regimes

We use the FEM-BV-VARX framework to classify flow regimes in the FLOSSII turbulence data. The turbulence data under consideration in Eq. (2) is the vertical velocity variance σ_w (defined in Section 2.2) and the external factor is the sub-mesoscale wind velocity V_{smeso} (Eq. 1). The clustering analysis is performed based on the data collected from the height of two meters. This choice ensures that the data are within the boundary layer, which can be very shallow in strongly stable conditions. Investigations of the height dependence of flow regimes is left for future work. Here instead, the scale interaction properties will be analysed at different heights assuming that the regime affiliation is the same for all heights.

User defined parameters of the framework include the maximum memory depth p for the forcing variable V_{smeso}, the number of possible distinct VARX models or cluster states K and the persistence parameter C_p, which limits the number of transitions between the states. The memory depth defines how many past states of the external factor V_{smeso} are used in the model in Eq. (2). The maximum memory lag that we use in this model is determined by a priori calculation of the partial autocorrelation function (*pacf*) for the variable V_{smeso} (Brockwell and Davis, 2002). The correlation between the time series drops on average after a few minutes, and is set to $p = 6$ (based on the average *pacf* over 68 nights). To determine the optimum number of K and C_p, multiple models are fitted for varied values of the parameters K and C_p.

In the clustering analysis of Vercauteren and Klein (2015), the optimal model parameters were chosen as the minimisers of the Akaike Information Criterion. However for the FLOSSII dataset, the AIC exhibits asymptotic behaviour towards zero for all models in the investigated parameter space ($K = 2, 3, 4, 5, 7$ and $C_p = [2, 302]$) and cannot be used as a selection criteria. Instead, the optimal model parameters are selected as those that minimise the correlation between the signal σ_w and the model residuals ϵ_t, while maximising the amount of variance of the signal explained by the model. By observing the change of these two quantities over the parameter space, we found that increasing the parameters beyond $K = 3$ and $C_p = 150$ did not reduce the correlation in the residuals and did not increase the modelled variance. Thus the choice of $K = 3$ and $C_p = 150$ is considered as an optimal model. The amount of variance of $\sigma_w(t)$ explained by the VARX model in the three clusters is 0.8%, 3% and 9.5%.

However, analysis of the model residuals showed that the error distribution in the cluster corresponding to the

largest explained variance was not Gaussian. This cluster has the most interaction between sub-mesoscales and vertical velocity fluctuations as shown by the larger explained variance and we want to classify the dynamical interactions more accurately. Therefore, we select the time series in this specific cluster and classify it with the FEM-BV-VARX methodology further into two distinct clusters. This strategy leads to error distributions that are closer to normally distributed in the two subsequent clusters. The reason why this two-step procedure is helpful to the regime classification can be understood in the following way. The clustering procedure is based on minimising the euclidean distance between the data and the statistical model, under the constraint that the number of transitions between cluster states are bounded (Horenko, 2010a). Since a large part of the FLOSSII data show little dynamical interactions between σ_w and V_{smeso} (with 0.8% resp. 3% explained variance), the mean part of the statistical model ($\mu(t)$ in (2)) has the strongest effect in the overall distance minimisation. Indeed, inspection of the data classified in three clusters show that those correspond in large part to different mean values of σ_w. The periods of largest interactions between σ_w and V_{smeso} also correspond to very stable flow regimes (Vercauteren and Klein, 2015) with the smallest mean values of σ_w and therefore these have the least weight in the distance minimisation. Selecting only those periods of larger dynamical interactions between σ_w and V_{smeso} enables a second level clustering which differentiates the dynamical interactions and not just the mean turbulent state. The fitted statistical models resulting from the two-step clustering strategy have a high degree of reproducibility. Over five repeated minimisation procedures for the FLOSSII data, the cluster affiliation function is consistent (or equal) to a degree of 90%.

As an indicator of the stability of the flow, we analyse the distributions of the bulk Richardson number

$$\mathrm{Ri}_b = (g/\Theta_0)\frac{(T(z_2) - T(z_1))\,\Delta z}{(V(z_2) - V(z_1))^2}, \tag{11}$$

in each cluster. Θ_0 is the potential temperature averaged over all sensors and over the time of record (1 minute), V is the record-averaged wind speed, T is the record-averaged potential temperature derived from the sonic anemometer measurements, $z_1 = 1$m and $z_2 = 10$m, Δz is the difference in height between the two levels and g is the gravitational acceleration. The Ri_b distributions conditional on the four identified flow regimes are shown in Fig. 2. The bins of the distributions are normalised with the number of samples in each regime to explain the relative probability. The clustering strategy is found to separate the Ri_b distributions into values indicative of weakly stable flows and strongly stable flows, albeit with large overlaps in the distributions. The distributions of C1, C2 and C3 are located well below the $\mathrm{Ri}_{b(\mathrm{crit})}$=0.25 and the boundary layer state at that times can be distinctly interpreted as weakly stable. The strongly stable cluster C4 shows a pronounced heavy tail decaying towards Ri_b=6 (not shown) and is showing a significant spread around the $\mathrm{Ri}_{b(\mathrm{crit})}$. When going from weakly stable cluster towards strongly stable clusters, the distribution of the Ri_b tends to diffuse, partly due to low values of the shear velocity that lead to uncertainties. The overlap of distributions and the diffused distribution of Ri_b highlights the difficulty of defining a threshold based on Ri_b for distinguishing flow regimes. As a note of caution, the distributions in Fig. 2 should be considered only as a qualitative indication of stability properties, since the temperature from the sonic anemometers are known to experience drift and biases between sensors exist, leading to uncertainties in the values. Hence we discard presenting a detailed analysis of the Ri distributions at each measurement height. Still, Fig. 2 shows that the clustering strategy, similarly to what was found in Vercauteren and Klein (2015), separates periods of qualitatively different stability according to Ri_b.

The clustering of the time series of σ_w using V_{smeso} as external factor is shown for an example period in Fig. 3, where the background colours denote regime affiliation. The middle horizontal panel show the first clustering procedure with three clusters. The Cluster (C3+C4) with the lowest mean is then considered as one continuous time series and clustered again to result in C3 and C4. The solution of this second clustering procedure is then denoted by the inserts panels. The cluster (C3+C4) is not considered for the following analysis and is shown here for explanatory reasons.

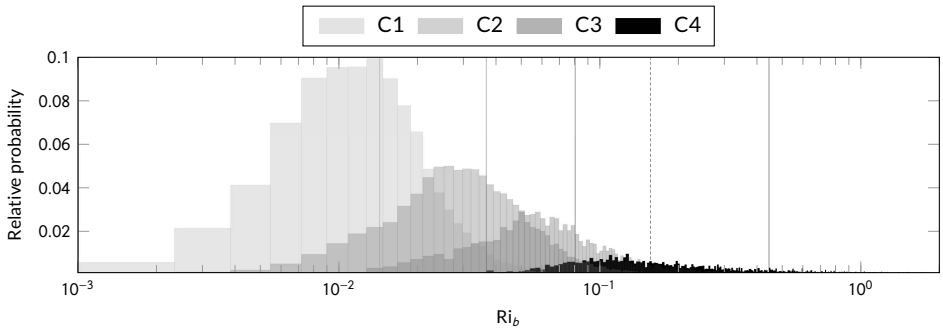

FIGURE 2 Histogram of the bulk Richardson numbers in the clustered flow regimes. Vertical lines representing the median of the underlying distribution. Going from left to right the values are: $Ri_{b(C1)}$=0.03, $Ri_{b(C2)}$=0.07, $Ri_{b(C3)}$=0.14, $Ri_{b(crit)}$=0.25, $Ri_{b(C4)}$=0.59. For better illustration of the distribution overlap the x-axis is showing a maximum $Ri_b = 2$. The heavy tail of the C4 distribution is reaching up to $Ri_{b(C1)} = 6$ and explaining the shifted value of the median.

By comparing the modelled time series between the middle panel and the inserts panels one will note, that for the strongly stable condition (namely comparing C3+C4 vs C3 and C4) the sub-clustered solution is describing the mean better compared to the C3+C4 solution. To resolve the mean with one level clustering we needed at least seven clusters. The solution with that amount of clusters started to be unreproducible, meaning the affiliation functions diverged for different solutions.

In the Fig. 3 the dynamics of σ_w is poorly captured by the model in the periods with more mixing (regimes C1 and C2). As a more quantitative indication of these differences, we compare the variance of the signal σ_w explained by the VARX models in each flow regime. While the amount of variance explained in C1 and C2 is very small (3%, 0.8% resp.), the model explains a larger amount in flow regimes C3 and C4 (around 10% for both). This difference denotes that the more stable cases show more interactions between turbulent and non-turbulent scales of motion.

To illustrate how the total heat flux and momentum flux is distributed among the scales of motion under different near-surface SBL conditions, the multi-resolution flux decomposition (MRD) cospectra are shown for the heights of 2 m, 20 m and 30 m in Fig. 4 (for the sensible heat fluxes) and Fig. 5 (for the momentum fluxes) for the four classified flow regimes C1-C4 (from left to right). The dashed vertical line shows the one minute average scale as a reference.

We first focus our observation on the lowest row of panels in Fig. 4, corresponding to the 2 m measurements. The sensible heat flux cospectra all have a negative peak, intuitively indicating the average scale of fluctuating vortices, followed by a decrease of the flux magnitude and levelling off of the heat flux for increasing averaging scales. The variability of the sub-mesoscales in a scale band from one minute to 30 minutes is approximately bounded between -3 and 3 Wm^{-2} with a median value close to zero for all four regimes. What is further visible is that going from C1 to C4 (increasing stability and submeso-turbulence interactions), the median amount of flux transported by the turbulent scales diminishes, peaking approximately at respectively -8 Wm^{-2}, -6 Wm^{-2}, -4 Wm^{-2}, -1 Wm^{-2} at a scale of one second. In C4 the magnitude of the turbulent scales start to intersect with the interquartile range of the sub-mesoscale band, denoting dynamics largely influenced by the sub-mesoscales. We continue investigating the heat flux by going to the next height.

In the middle row of the Fig. 4 we observe the heat flux cospectra at a height of 15 meter. The behaviour of the cospectra along the four regimes exhibits changes similar to those discussed for the 2 m fluxes, with the following differences. Going from C1 to C4 (from left to right) the average amount of flux transported by the turbulent scales diminishes faster than at the height of two meters. Furthermore the scale of the negative peak is increasing ($\approx$ 4 s).

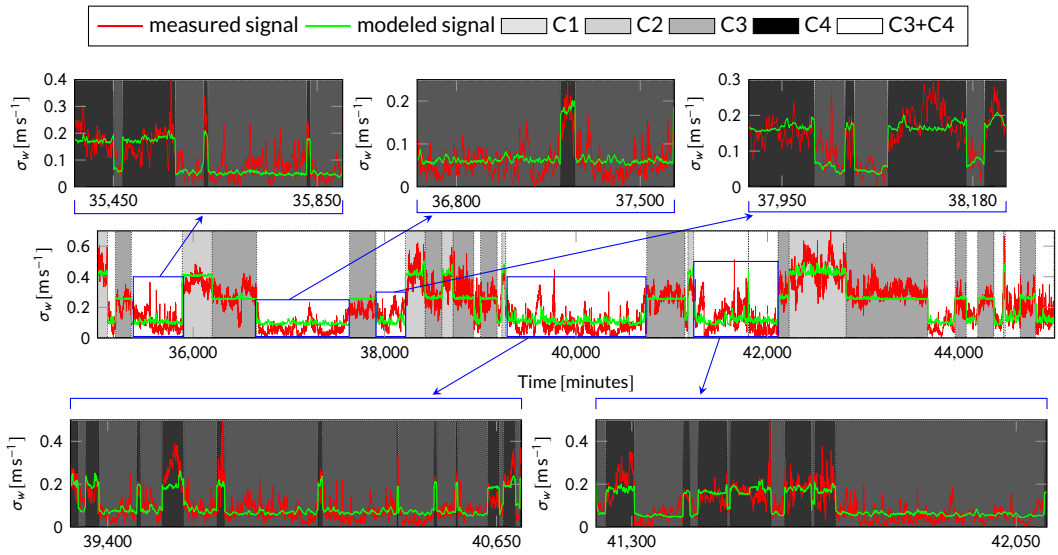

FIGURE 3 Example of timeseries and flow regimes. The middle horizontal panel is showing a period of 68 nights. The inserts explaining the solution produced by the second application of the clustering methodology.

Compared to height of two meters the variability of the sub-mesoscales is now higher ± 5 Wm^{-2}, and reaches even ± 8 Wm^{-2} in C3. In C4 the interquartile range of the sub-mesoscale band is broader than the interquartile range of the sub-mesoscale band at 2 m. This together with the higher diminishing rate of the turbulent scales indicates an increased influence of the sub-mesoscales relative to the lower height.

In the upper panels row of the Fig. 4 we observe the change of the heat flux cospectra at a height of 30 meter. Similar to observations from lower levels we note a further increase of the sub-mesoscale variability, reaching values of more then ± 6 Wm^{-2}. In summary the variability of the sub-mesoscales is decreasing by getting closer to the ground. In C1 the turbulent scales are dominant over all heights, while in C4 the sub-mesoscales variability is dominant. The relative contribution of the sub-mesoscales to the overall transport increases with increasing regime affiliation number for all heights.

The momentum flux cospectra in Fig. 5 obeys a similar pattern across the regimes as the heat flux cospectra in Fig. 4. In C1 the turbulent scales are dominant. But as we approach C4 the sub-mesoscale variability start to be dominant. The sub-mesoscale variability also decreases with height. Although the heat cospectra and the momentum cospectra are almost identical in their evolution in parameter space of regime and height we can observe one major difference. As we go column wise from regime C1 to C4, the sub-mesoscale variability in the heat cospectra (Fig. 4) have a tendency to increase, where in the momentum cospectra they have a tendency to decrease. Therefore with increasing stability the ratio of intermittent heat transport to momentum transport by sub-mesoscales is rising.

3.2 | Anisotropy characteristics in different flow regimes

Having classified flow regimes according to the interactions between sub-mesoscales and turbulent scales and characterised the scales transport properties, we can now turn to the analysis of anisotropy characteristics in the different flow regimes. In order to calculate the anisotropy tensor (Eq. 4) and its invariants, an averaging scale has to be defined.

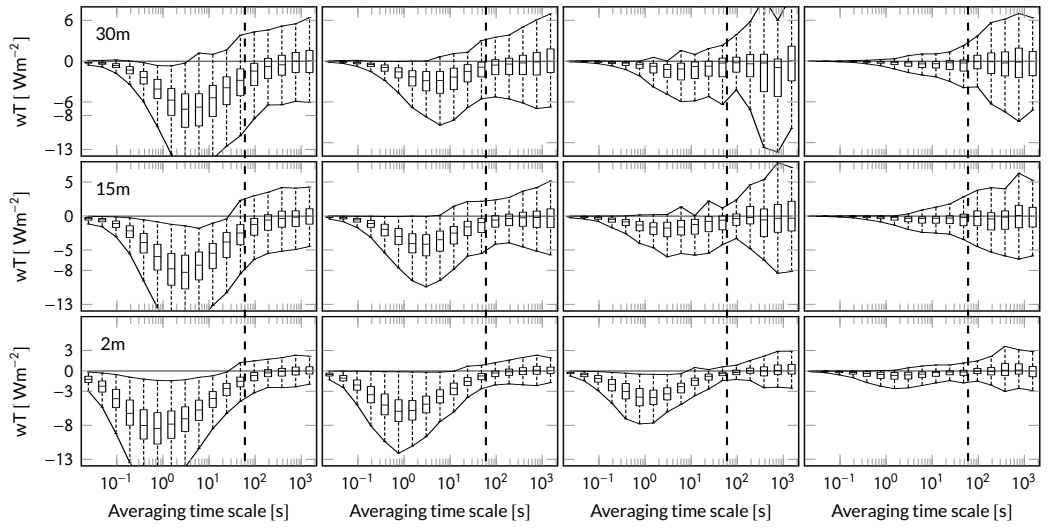

FIGURE 4 MRD heat flux cospectra. Observing from top to bottom, every row of panels is corresponding to height of 30 meters, 15 meters and two meter respectively. Observing from left to right, every column of panel is corresponding to regimes C1-C4 respectively. Where C1 is a weakly stable regime and C4 is a strongly stable regime. The major dashed vertical lines in every panel are marking the one minute scale. Each panel contains 17 box plots, each of them representing the distribution of the wT on a corresponding scale. The boxes are representing the 25th and 75th percentiles, where the whiskers across the scales are connected with a solid line. The horizontal line in each box shows the median.

From the MRD results in Fig. 4 it appears that the heat flux cospectra level-off at averaging times ranging between approximately 5 minutes (C1) and 1 minute (C4), depending on how strongly stable the flow regime is. In order to minimize contributions from sub-mesoscale motions in the anisotropy analysis, we select the shortest averaging timescale of 1 minute as was done in Stiperski and Calaf (2018). Note that this choice implies that the anisotropy analysis will discard some of the turbulent contributions to anisotropy tensor in the less stable flow regimes.

The distribution of anisotropy states is shown for each cluster C1-C4 and each measurement height in Fig. 6, where the gray scale shows the density of points. While mixed states of anisotropy, i.e. towards the middle of the barycentric map, are the most common in all cases, marked differences appear in the limiting states. Here we follow Stiperski and Calaf (2018) to define limiting "pure" states of anisotropy as states falling in edges of the barycentric map, where the limiting lines for each edge were chosen to cover 70 % of the sides of the equilateral triangle as illustrated in Fig. 1. The isotropic states corresponds to the upper corner of the barycentric map. A height dependance is clearly apparent here. Isotropic stresses are indeed only found away from the ground, and the higher levels have the highest densities of isotropic stresses, regardless of flow regime affiliations. This result is not surprising because the presence of the ground surface enhances the shear distortion effects on the turbulence, and was discussed elsewhere (e.g. Antonia and Krogstad (2001)). The shear effects in the absence of thermal stratification would, however, lead to two-component stresses. While all stresses appear closer to axisymetric stresses when one approaches the ground surface, clearly the preference is towards one-component stresses. This preference depends on regime affiliation.

Indeed, the density of stresses in the one-component limiting states becomes higher for increasing regime affiliation number (Fig. 6) corresponding to increasingly stable conditions (Fig. 2), and increasing influence of sub-mesoscale motions as discussed above. We specifically quantify the percentage of stresses falling in each limiting state of anisotropy

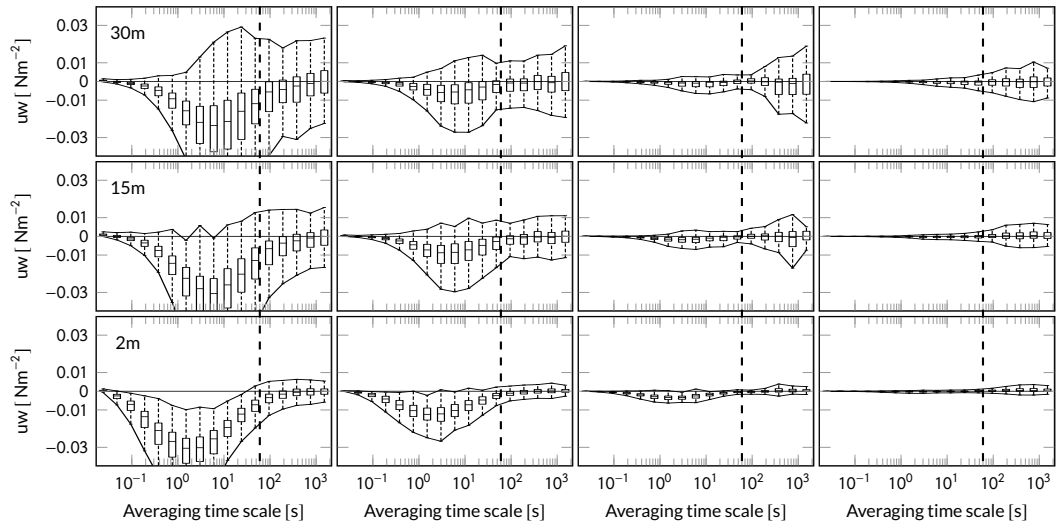

FIGURE 5 MRD momentum flux cospectra. Observing from top to bottom, every row of panels is corresponding to height of 30 meters, 15 meters and two meter respectively. Observing from left to right, every column of panel is corresponding to regimes C1-C4 respectively. Where C1 is a weakly stable regime and C4 is a strongly stable regime. The major dashed vertical lines in every panel are marking the one minute scale. Each panel contains 17 box plots, each of them representing the distribution of the uw on a corresponding scale. The boxes are representing the 25th and 75th percentiles, where the whiskers across the scales are connected with a solid line. The horizontal line in each box shows the median.

in Fig. 7, conditionally on regime affiliation and height of measurement. The isotropic edge (black bar in the figure) is almost absent until the measurement height of 5 m, and then the proportion of isotropic stresses increases with height for all flow regimes, having almost the same proportion in all regimes (with the maximum at 30 m of slightly less than 10 %). The proportions of two-component stresses show an opposite trend, decreasing with height but being also very similar for all flow regimes. The proportions of one-component stresses also decreases for increasing heights, but here the regime dependence is strong. In C1 and C2, the proportions of one-component stresses is very small at all heights, while it is large in C3 and even large in C4, reaching almost 30 % of the states near the surface. In these regimes, the turbulent contribution to the heat flux cospectra is not very large, and the contributions due to sub-mesoscales are comparable to (C3) or more important than (C4) the turbulence contributions (Fig. 4). Since the activity of these sub-mesoscales occurs on scales just above or similar to the largest turbulent scales, the turbulence is probably not in equilibrium with the sub-mesoscale motions in the sense that it may not have lost memory its the larger scale anisotropic forcing mechanism.

In order to faciliate interpretation of the one-component stresses in the physical space, we calculate the non-dimensional velocity aspect ratio (VAR) for the limiting one-component stresses and for all other cases separately. This ratio takes the value of one if all three standard deviations approach the same value and is defined by Mahrt et al. (2012a) as:

$$VAR \equiv \frac{\sqrt{2}\sigma_w}{\sqrt{\sigma_u^2 + \sigma_v^2}}. \tag{12}$$

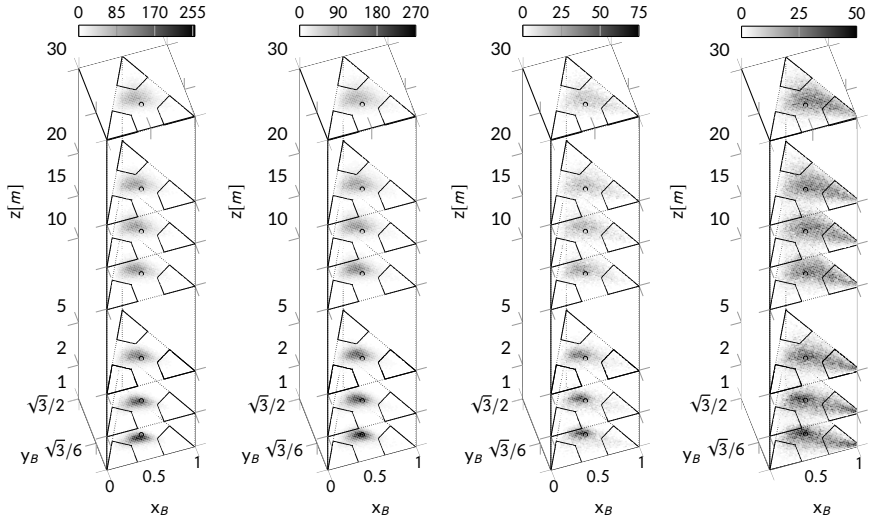

(a) Cluster 1 (b) Cluster 2 (c) Cluster 3 (d) Cluster 4

FIGURE 6 Anisotropy as states in the barycentric map for each height and flow regime. The colourbar shows the density of points in each state of the barycentric map.

In Tab. 1 we evaluate the mean value of the VAR in each regime for cases corresponding to the one-component anisotropy state and compare it to mean value of VAR for the time that are not in the one-component anisotropy state. As we change the regime from C1 to C4 we observe a decrease of the VAR from 0.10 to 0.07, along with an increase of the standard deviation of VAR. In comparison, the ratio for cases outside the one-component limit is not dropping below 0.20. Thus the vertical component of the Reynolds stress is smallest for the one-component cases, and reduces for increasing regime affiliation number. This may partly be due to horizontal submeso motions reaching scales below the one-minute in the most stable flow regimes.

TABLE 1 Mean and standard deviation of VAR for one-component (top row) and non one-component (bottom row) anisotropy state along the regimes C1-C4 at height of two meters.

component	C1	C2	C3	C4
one	0.10 ± 0.03	0.10 ± 0.03	0.09 ± 0.04	0.07 ± 0.05
non one	0.20 ± 0.05	0.23 ± 0.05	0.23 ± 0.07	0.20 ± 0.10

3.3 | Anisotropy characteristics of counter gradient cases

Interactions between waves or sub-mesoscale motions and turbulence have been shown to lead to counter-gradient fluxes (Einaudi and Finnigan, 1993). In Fig. 8, we separate the stresses falling in the flow regime C4 into two categories, namely periods of negative sensible heat flux (on one minute averaging scale) and periods of positive (counter-gradient) sensible heat flux as shown in Fig. 8(b). To separate the anisotropic state in Fig. 8(c) and Fig. 8(a) we use the heat flux $\overline{w'T'}$ averaging scale of one minute. The peak of the density of anisotropy states for the cases of negative sensible

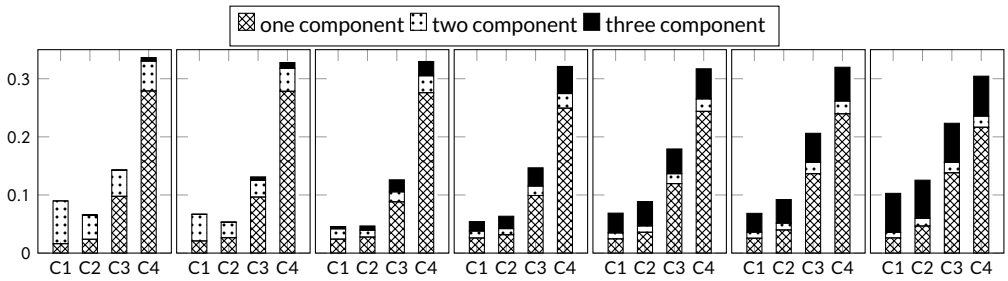

FIGURE 7 Occurrences of each anisotropy states for different heights and clusters. Left to right: 1, 2, 5, 10, 15, 20 and 30 m above ground. The numbers 1,2,3,4 denote the flow regime affiliations C1-C4. The length of the bar represents the percentage of stresses within each edge. Isotropic, two-component axisymmetric, one-component. The pure states are defined as in Fig. 1.

TABLE 2 Percentage of cases of negative (+g for with gradient) and positive (-g for counter gradient) sensible heat flux (one minute scale) observed in the one component limiting anisotropy state (right corner of the barycentric map). For the column 'total' no affiliation function is involved. The affiliation function to determine regimes C1-C4 is calculated based on height of two meters and is used to evaluate the table entries for all heights.

	C1	C2	C3	C4	total
height [m]	+g [%] / -g [%]	+g [%] / -g [%]	+g [%] / -g [%]	+g [%] / -g [%]	+g [%] / -g [%]
30	84.56/15.44	86.17/13.83	83.87/16.13	86.67/13.13	85.88/14.12
15	90.34/9.66	90.79/9.21	89.15/10.85	91.53/8.47	90.95/9.05
2	97.24/2.76	93.96/6.04	97.69/2.31	96.20/3.80	96.17/3.82

heat flux (with-gradient) occurs in the middle of the barycentric map. In the counter-gradient cases however, the peak of the distribution lies within the edge corresponding to the one-component limiting states. Hence, most of the counter-gradient cases correspond to one-component limiting states. In order to analyse if the reverse is true, i.e. if one-component limiting states are mainly counter-gradient cases, the percentage of cases with positive and negative sensible heat flux is listed in Tab. 2 for all one-component limiting states in each flow regime C1-C4. The values show that only a small proportion of the cases in one-component limiting states correspond to positive sensible heat flux, and that the percentage is similar for all flow regimes.

From these observations, we speculate that counter gradient cases are potentially associated with submeso motions occurring on scales below 1 minute, which explain the one-component signature of the Reynolds stresses in these cases. Nevertheless, it is not possible to associate one-component turbulence with a specific set of submeso motions which would cause counter gradient fluxes.

3.4 | Dynamical indicators in the anisotropy dynamics

We now turn to the analysis of the dynamics of the states of anisotropy. We want to investigate if the rate of isotropisation depends on the initial anisotropy state, and on the background flow regime. Moreover we are interested in assessing the trajectories of the stresses in the anisotropy invariant coordinates. Based on the timeseries of the anisotropy invariant coordinates x_B and y_B, we estimate the persistence and dimension of the dynamics as presented in

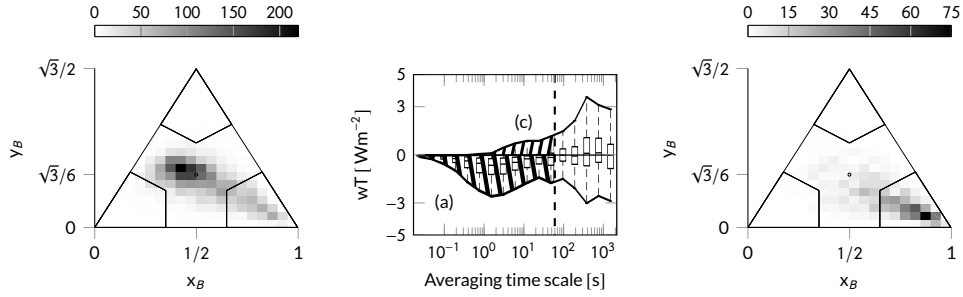

(a) With gradient. (b) Heat Flux cospectrum. (c) Counter gradient.

FIGURE 8 Anisotropy dependence on the sign of sensible heat flux (b) in C4 regime on height of two meters. In (a) and in (c) the color map is showing the density of points.

section 2.5. Figure 9 shows a scatterplot of the persistence indicator θ estimated from the parameter of the distribution in Eq. 10, the colour showing the value of the indicator. It is obvious that θ values are smaller in the edge corresponding to one-component stresses, denoting longer-lived states. We recall that values close to $\theta = 1$ imply that the trajectory immediately leaves the initial anisotropy state, while smaller values denote that the dynamics resides in a neighbourhood of the initial state. In the mixed states in the centre of the barycentric maps, the indicator values are very close to 1 denoting that those states are modified almost instantaneously. The longer-lived one-component stresses is in accordance to what was found in Choi and Lumley (2001) for homogeneous turbulence.

We calculate the estimates of the local dimension of the dynamics based on Eq. 9, for each stress and show the scatterplot of the estimated dimensions in Fig. 10. The maximum local dimension is two, since the phase-space is the plane formed by the eigenvectors, i.e. x_B and y_B. A local dimension of two indicates that there is no preferred direction in which the anisotropy state is altered; it can change in any direction on the plane, starting in an initial state. On the contrary, a smaller local dimension indicates that the way that the anisotropy state is modified occurs in a restricted part of the plane, that is, with a preferred direction. This is evidently the case close to the one-component edge of the barycentric map, and along a line connecting the one-component edge to the centre of the map. This denotes a preferential path away or towards one-component anisotropy. It is interesting to note that this preferential path does not include or evolve towards two-component axisymmetric states Stiperski and Calaf (2018), but shows that intermittent bursts of turbulence are mostly of axisymmetric oblates, with a more pronounced third direction.

The combination of persistence and dimension analysis possibly shows that one-component stresses are more stable topologically, and that the formation or destruction of such topological structures takes a preferential route.

4 | CONCLUSIONS

We classified SBL flow regimes based on interaction properties between the sub-mesoscale wind velocity and the turbulent velocity fluctuations and analysed the anisotropy properties of the Reynolds stress tensor in each flow regime. The combination of methods highlighted different properties of the turbulent stresses under the influence of submeso motions. We showed that the influence of submeso motions on the turbulence gains significance as the stability increases, and that the more submeso-influenced flow regimes have a marked preference for one-component axisymmetric stresses. This topological signature is in part resulting from the buoyancy damping effects, but also from

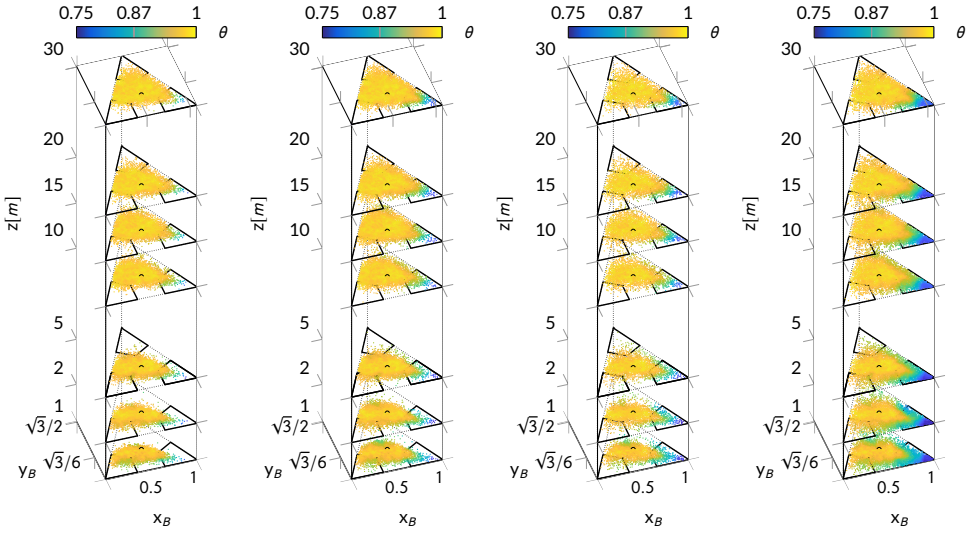

(a) C1 (b) C2 (c) C3 (d) C4

FIGURE 9 Persistency of the dynamics of the anisotropy state. The colourbar is indicating the value of θ, where low values correspond to high persistence of the trajectory in the neighbourhood and values close to 1 imply that the trajectory immediately leaves the sphere.

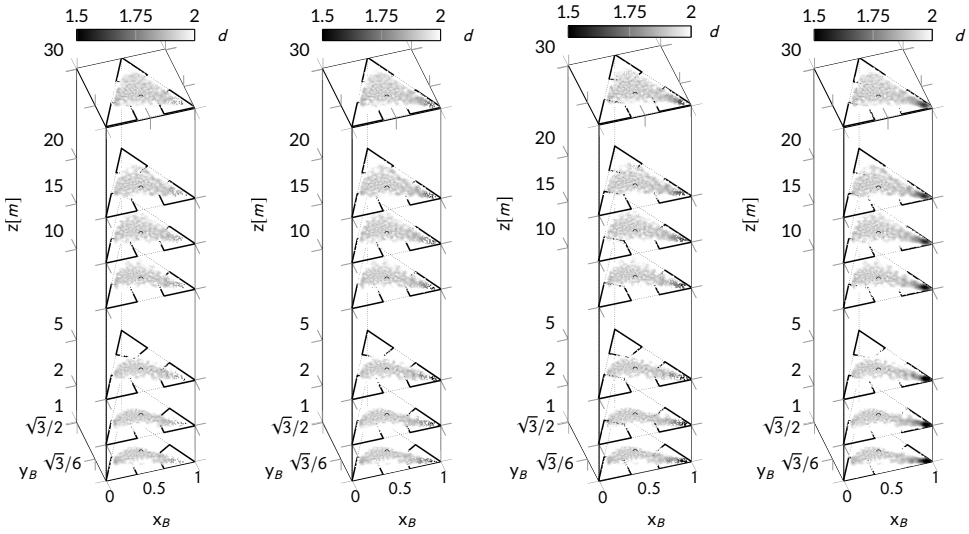

(a) C1 (b) C2 (c) C3 (d) C4

FIGURE 10 Local dimension of the anisotropy states.

the influence of submeso scale forcing of turbulence. Indeed we found that a large proportion of the periods where the sensible heat flux was against the mean downward gradient, typically corresponding to submeso motions, was characterised by one-component limiting states of anisotropy. However, only a small fraction of all one-component limiting cases happen during counter-gradient periods. Close to the surface (below 2 m), the effect of shear appeared to compete with buoyancy damping effect, resulting in a significant proportion of two-component axisymmetric stresses - a typical signature of shear induced turbulence. Isotropic stresses were found at higher levels in all flow regimes, when shear effects are no longer felt by the small scale turbulence.

The results show, in line with the findings of Stiperski and Calaf (2018), that the one-component turbulence topology is associated with predominantly horizontal motions and is most common in very stable conditions, that still allow the development of intermittent turbulent bursts of almost isotropic type. Indeed Stiperski and Calaf (2018) showed that in very stable conditions, when turbulence at 30 min scale was one-component or two-component axisymmetric, close to isotropic turbulence at smaller scales can still be initiated. This type of turbulence is associated with bursts. The present results are unable to elucidate the differences between the one-component and two-component turbulence found by Stiperski and Calaf (2018), but show that the proportion of one-component cases increases for increasing importance of the sub-mesoscales dynamics.

Additionally we showed that one-component stresses were more persistent in their dynamics, and highlighted signs of a preferred route towards or away from one-component stresses in the topological state space. This route interestingly does not involve purely two-component axisymmetric turbulence, but is more of a axisymmetric oblate type. An interesting future analysis would be to investigate the scale-wise return to isotropy in parallel with our results on the persistence and dimension of the dynamics.

The results can be used to improve the representation of non-stationary turbulence under the influence of sub-mesoscale motions. This is pertinent for subgrid-scale turbulent parameterisation, which are currently mainly based on isotropic eddy diffusivity models. Our results show that anisotropic modelling is required in cases where the variability of sub-mesoscales is important in relation to the turbulent scales. The signs for a preferred route towards or away from the one-component stresses despite strong influence of random sub-mesoscale motions provide encouraging perspectives for representing the return-to-isotropy in future models.

ACKNOWLEDGEMENTS

The authors would like to thank Marc Calaf for inspiring discussions at an early stage of this analysis. Larry Mahrt is acknowledged for providing the FLOSSII data and his help to analyse them. Illia Horenko and Dimitri Igdalov provided the FEM-BV-VARX framework and help that was greatly appreciated. The research was funded by the Deutsche Forschungsgemeinschaft (DFG) through grant number VE 933/2- 1, and benefited from the inspiring research environment of the DFG-funded Collaborative Research Center CRC1114, "Scaling Cascades in Complex system" through the project B07. The exchanges between N.V and D.F were greatly facilitated by funding through the DAAD exchange program Procope through the project "Data-driven dynamical stability of stably stratified turbulent flows". The work of Ivana Stiperski was funded by Austrian Science Fund (FWF) grant T781-N32. Davide Faranda acknowledges support from the ERC grant No. 338965-A2C2.

CONFLICT OF INTEREST

The authors declare no conflict of interests.

REFERENCES

Acevedo, O. C., Mahrt, L., Puhales, F. S., Costa, F. D., Medeiros, L. E. and Degrazia, G. A. (2015) Contrasting structures between the decoupled and coupled states of the stable boundary layer. *Quarterly Journal of the Royal Meteorological Society*, **142**, 693–702.

Antonia, R. and Krogstad, P. A. (2001) Turbulence structure in boundary layers over different types of surface roughness. *Fluid Dynamics Research*, **28**, 139–157.

Banerjee, S., Krahl, R., Durst, F. and Zenger, C. (2009) Presentation of anisotropy properties of turbulence, invariants versus eigenvalue approaches. *Journal of Turbulence*, **8**, N32–28.

Belušić, D. and Güttler, I. (2010) Can mesoscale models reproduce meandering motions? *Quarterly Journal of the Royal Meteorological Society*, **136**, 553–565.

Brockwell, P. J. and Davis, R. A. (2002) *Introduction to Time Series and Forecasting*. Springer, 2nd edn.

Brugger, P., Katul, G. G., De Roo, F., Kröniger, K., Rotenberg, E., Rohatyn, S. and Mauder, M. (2018) Scalewise invariant analysis of the anisotropic Reynolds stress tensor for atmospheric surface layer and canopy sublayer turbulent flows. *Physical Review Fluids*, **3**, 163.

Cava, D., Mortarini, L., Giostra, U., Richiardone, R. and Anfossi, D. (2016) A wavelet analysis of low-wind-speed submeso motions in a nocturnal boundary layer. *Quarterly Journal of the Royal Meteorological Society*, **143**, 661–669.

Choi, K.-S. and Lumley, J. L. (2001) The return to isotropy of homogeneous turbulence. *Journal of Fluid Mechanics*, **436**, 59–84.

Eckmann, J.-P. and Ruelle, D. (1985) Ergodic theory of chaos and strange attractors. In *The Theory of Chaotic Attractors*, 273–312. Springer.

Einaudi, F. and Finnigan, J. J. (1993) Wave-Turbulence Dynamics in the Stably Stratified Boundary-Layer. *Journal of Atmospheric Sciences*, **50**, 1841–1864.

Faranda, D., Messori, G. and Yiou, P. (2017a) Dynamical proxies of North Atlantic predictability and extremes. *Scientific Reports*, 1–10.

Faranda, D., Sato, Y., Saint-Michel, B., Wiertel, C., Padilla, V., Dubrulle, B. and Daviaud, F. (2017b) Stochastic chaos in a turbulent swirling flow. *Physical review letters*, **119**, 014502.

Holtslag, A., Tjernström, M., Basu, S., Beljaars, A. C. M., Svensson, G., Baas, P., Beare, B., Bosveld, F. C., Cuxart, J., Lindvall, J., Steeneveld, G. J. and van de Wiel, B. J. H. (2013) Stable Atmospheric Boundary Layers and Diurnal Cycles: Challenges for Weather and Climate Models. *Bulletin of the American Meteorological Society*, **94**, 1691–1706.

Horenko, I. (2010a) On clustering of non-stationary meteorological time series. *Dynamics of Atmospheres and Oceans*, **49**, 164–187.

— (2010b) On the Identification of Nonstationary Factor Models and Their Application to Atmospheric Data Analysis. *Journal of Atmospheric Sciences*, **67**, 1559–1574.

Kang, Y., Belušić, D. and Smith-Miles, K. (2015) Classes of structures in the stable atmospheric boundary layer. *Quarterly Journal of the Royal Meteorological Society*, **141**, 2057–2069.

Lang, F., Belušić, D. and Siems, S. (2017) Observations of Wind-Direction Variability in the Nocturnal Boundary Layer. *Boundary-Layer Meteorology*, 1–18.

Lucarini, V., de Freitas, A. C. G. M. M., Faranda, D., Freitas, J. M., Holland, M., Kuna, T., Nicol, M., Todd, M. and Vaienti, S. (2016) *Extremes and Recurrence in Dynamical Systems*. John Wiley & Sons.

Lumley, J. L. (1978) Computational modeling of turbulent flows. **18**, 123 – 176. URL: http://www.sciencedirect.com/science/article/pii/S0065215608702667.

Lumley, J. L. and Newman, G. R. (1977) The return to isotropy of homogeneous turbulence. *Journal of Fluid Mechanics*, **82**, 161–178.

Mahrt, L. (2011) The Near-Calm Stable Boundary Layer. *Boundary-Layer Meteorology*, **140**, 343–360.

— (2014) Stably Stratified Atmospheric Boundary Layers. *Annual Review of Fluid Mechanics*, **46**, 23–45.

Mahrt, L., Richardson, S. J., Seaman, N. and Stauffer, D. R. (2012a) Turbulence in the nocturnal boundary layer with light and variable winds. *Quarterly Journal of the Royal Meteorological Society*, **138**, 1430–1439.

Mahrt, L. and Thomas, C. K. (2016) Surface Stress with Non-stationary Weak Winds and Stable Stratification. *Boundary-Layer Meteorology*, **159**, 3–21.

Mahrt, L., Thomas, C. K., Richardson, S. J., Seaman, N., Stauffer, D. R. and Zeeman, M. J. (2012b) Non-stationary Generation of Weak Turbulence for Very Stable and Weak-Wind Conditions. *Boundary-Layer Meteorology*, **147**, 179–199.

Mahrt, L. and Vickers, D. (2005) Boundary-layer adjustment over small-scale changes of surface heat flux. *Boundary-Layer Meteorology*, **116**, 313–330.

Messori, G., Caballero, R. and Faranda, D. (2017) A dynamical systems approach to studying midlatitude weather extremes. *Geophysical Research Letters*, **44**, 3346–3354.

Moreira Freitas, A. C., Freitas, J. M. and Todd, M. (2010) Hitting time statistics and extreme value theory. *Probability Theory and Related Fields*, **147**, 675–710.

Mortarini, L., Cava, D., Giostra, U., Acevedo, O. C., Nogueira Martins, L. G., Soares de Oliveira, P. E. and Anfossi, D. (2017) Observations of submeso motions and intermittent turbulent mixing across a low level jet with a 132-m tower. *Quarterly Journal of the Royal Meteorological Society*, **144**, 172–183.

O'Kane, T. J., Risbey, J. S., Monselesan, D. P., Horenko, I. and Franzke, C. L. E. (2016) On the dynamics of persistent states and their secular trends in the waveguides of the Southern Hemisphere troposphere. *Climate Dynamics*, **46**, 3567–3597.

Pope, S. B. (2000) *Turbulent Flows*. Cambridge University Press.

Risbey, J. S., Monselesan, D. P., Franzke, C. L. E., Horenko, I. and O'Kane, T. J. (2015) Metastability of Northern Hemisphere Teleconnection Modes. *dx.doi.org*.

Sandu, I., Beljaars, A. C. M., Bechtold, P., Mauritsen, T. and Balsamo, G. (2013) Why is it so difficult to represent stably stratified conditions in numerical weather prediction (NWP) models? *Journal of Advances in Modeling Earth Systems*, **5**, 117–133.

Sarkar, S. (2003) The effect of stable stratification on turbulence anisotropy in uniformly sheared flow. *Computers & Mathematics with Applications*, **46**, 639–646.

Smyth, W. D. and Moum, J. N. (2000) Anisotropy of turbulence in stably stratified mixing layers. *Physics of Fluids (1994-present)*, **12**, 1343–1362.

Stiperski, I. and Calaf, M. (2018) Dependence of near-surface similarity scaling on the anisotropy of atmospheric turbulence. *Quarterly Journal of the Royal Meteorological Society*, 1–17.

Sun, J., Lenschow, D. H., Burns, S., Banta, R. M., Newsom, R., Coulter, R., Nappo, C. J., Frasier, S., Ince, T. and Balsley, B. B. (2004) Atmospheric disturbances that generate intermittent turbulence in nocturnal boundary layers. *Boundary-Layer Meteorology*, **110**, 255–279.

Sun, J., Mahrt, L., Nappo, C. J. and Lenschow, D. H. (2015) Wind and Temperature Oscillations Generated by Wave–Turbulence Interactions in the Stably Stratified Boundary Layer. *Journal of Atmospheric Sciences*, **72**, 1484–1503.

Vercauteren, N. and Klein, R. (2015) A Clustering Method to Characterize Intermittent Bursts of Turbulence and Interaction with Submesomotions in the Stable Boundary Layer. *Journal of the atmospheric sciences*, **72**, 1504–1517.

Vercauteren, N., Mahrt, L. and Klein, R. (2016) Investigation of interactions between scales of motion in the stable boundary layer. *Quarterly Journal of the Royal Meteorological Society*, **142**, 2424–2433.

Vickers, D. and Mahrt, L. (2003) The cospectral gap and turbulent flux calculations. *Journal of atmospheric and oceanic technology*, **20**, 660–672.